RSC Advances

PAPER

View Article Online
View Journal | View Issue

Cite this: *RSC Adv.*, 2024, **14**, 19912

Preparation and application of alkali-activated cementitious materials in solidification/stabilization of chromite ore processing residue†

Pengyue Su,‡[a] Pan Zhao,‡[a] Hao Wang,[a] Kun Zhou,[a] Yicheng Guo,[a] Sha Liu,[a] Huicheng Lu,[a] Haiyu Chen,[a] Lanjun Zhang,[a] Ziqiang He,[e] Ming Xia *[abc] and Shujie Zhao*[d]

Chromite ore processing residue (COPR) is a typical hazardous waste, which contains Cr(VI) and poses a great threat to the ecological environment and human health. In this study, solidification/stabilization (S/S) of COPR was carried out by using blast furnace slag (BFS) and fly ash (FA) to prepare alkali-activated cementitious materials (AACM). The influence of different factors (water glass modulus, liquid–solid ratio, alkali–solid content and curing temperature) on compressive strength was investigated by single-factor experiment. Additionally, solidification effect of AACM was determined according to the compressive strength and the leaching concentration of chromium (Cr(VI) and total Cr). According to the optimal conditions of the single-factor experiment, the highest compressive strength of 147.6 MPa was obtained after using the water glass modulus 1.0, liquid–solid ratio 0.28, alkali–solid content 8%, curing temperature 45 °C. The COPR was solidified in the AACM sample having highest compressive strength. The solidified body still has a good mechanical property (38.2 MPa) with 60% addition COPR. According to leaching tests, the leaching of Cr(VI) and total Cr of solidified body with 50% COPR was far lower than the limit value, which met the purpose of construction and landfill disposal. X-ray diffraction (XRD) analysis, Fourier transform infrared spectroscopy (FTIR) and scanning electron microscopy (SEM) analysis proved that heavy metal chromium was solidified in AACM by physical and chemical means.

Received 19th February 2024
Accepted 15th June 2024

DOI: 10.1039/d4ra01270d

rsc.li/rsc-advances

1. Introduction

Chromite ore processing residue (COPR) is a toxic and harmful waste residue generated in the process of producing chromium salts. COPR contains a significant amount of water-soluble and acid-soluble hexavalent chromium ions, constituting a substance that causes teratogenic, carcinogenic, and mutagenic effects, whose leaching toxicity far exceeds that of relatively stable trivalent chromium ions.[1] Unreasonable stacking or irregular treatment of COPR will severely pollute soil and groundwater, posing a significant threat to human health. Therefore, it is necessary to carry out resource-based disposal of COPR.

Currently, various methods have been used to handle hazardous wastes, such as thermal treatment technology,[2–4] chemical neutralization and extraction separation technology,[5–7] biological treatment technology[8–10] and solidification/stabilization (S/S) technology.[1,11] The technical advantages and disadvantages were shown in Table 1. The United States Environmental Protection Agency (USEPA) has highlighted that S/S is regarded as the best treatment technology due to its high efficiency in the treatment of hazardous waste.[1,12,13]

In the early stages, ordinary Portland cement (OPC) was widely utilized to S/S hazardous waste due to its high compressive strength, but its high energy consumption and poor stability for chromium stabilization limit its application. In a bid to enhance cement properties and mitigate carbon emissions, French chemist Joseph Davidovits initially introduced the concept of geopolymers during 1979.[14] This novel alkali-activated cementitious material (AACM) is primarily produced by combining general solid wastes abundant in Si, Al, and Ca (such as Fly Ash (FA), Blast Furnace Slag (BFS), metakaolin, *etc.*) with alkaline activators (Na_2SiO_3, NaOH, KOH, or

[a]*School of Environmental and Chemical Engineering, Jiangsu Ocean University, Lianyungang, 222005, China. E-mail: xiaming@jou.edu.cn*

[b]*Jiangsu Institute of Marine Resources Development, Jiangsu Ocean University, Lianyungang, 222005, China*

[c]*Jiangsu Key Laboratory of Function Control Technology for Advanced Materials, Jiangsu Ocean University, Lianyungang, 222005, China*

[d]*School of Safety Science and Engineering, Anhui University of Science and Technology, Huainan, 232001, China. E-mail: zsj9506@163.com*

[e]*Key Laboratory of Electromechanical Equipment Security in Western Complex Environment for State Market Regulation, Chongqing Special Equipment Inspection and Research Institute, Chongqing, 401121, China*

† Electronic supplementary information (ESI) available. See DOI: https://doi.org/10.1039/d4ra01270d

‡ These authors contributed equally to the work.

Table 1 The comparison of methods for handling hazardous wastes

Methods	Advantages	Disadvantages
Thermal treatment technology	Thorough treatment; volume reduction	High energy consumption; high equipment demands; air pollution
Chemical neutralization and extraction separation technology	Rapid and efficient; wide applicability	Secondary pollution; high cost; complex process
Biological treatment technology	Environmentally friendly; low cost; adaptable	Long treatment time; environmental dependency; limited range
Solidification/stabilization (S/S) technology	Long-term stability; simple operation; versatile materials	High cost of materials; large space consumption; long-term monitoring required

K_2SiO_3) to initiate a hydration reaction, forming a hydrated aluminum silicate gel.[15] Subsequently, it gradually solidifies through further hydration reaction and polycondensation, leading to the formation of the rigid structure.

Numerous researchers have observed the effective solidification of heavy metals through AACM. Xia *et al.* 2019 (ref. 13) had achieved successful heavy metal solidification of Cr, Cu, Zn, and Pb derived from lead and zinc smelting slag (LZSS) by creating composite AACM using BFS and FA. Zhang *et al.* 2020 (ref. 16) had employed LZSS as a primary material to produce AACM, achieving self-cementation solidification of its heavy metals in the current study. Similarly, Zhao *et al.* 2022 (ref. 17) had effectively solidified heavy metals, including Cr, As, and Pb, which present in lead smelting slag (LSS) by AACM, obtaining a relatively high compressive strength of 47.1 MPa. Xing and Wang 2023 (ref. 18) had solidified heavy metals from municipal solid waste incineration fly ash using AACM, and pointed out the augmentation of C–(A)–S–H gel content and structural modifications within the solidified body had fostered increased compressive strength. Reduced pore size had reinforced the physical encapsulation of heavy metals and had diminished their leaching toxicity over extended curing periods.

BFS is one kind of waste residue generated during the blast furnace ironmaking in steel mills, while FA is the residue recovered and extracted from the flue gas of coal-fired power plants. The preparation process of BFS-AACM (preparation of AACM using BFS) primarily involves the dissolution of Ca and Al participation to form a C–(A)–S–H type gel structure ($CaO–Al_2O_3–SiO_2–H_2O$).[19,20] On the other hand, FA-AACM (preparation of AACM using FA) achieves strength development through the formation of a three-dimensional 'N–A–S–H' type gel ($NaO_2–Al_2O_3–SiO_2–H_2O$).[1,21] Typically, BFS-AACM tends to encounter issues such as poor workability, short setting time, and significant shrinkage. Similarly, FA-AACM also suffers from drawbacks like low reactivity.[21,22] Existing studies have demonstrated that utilizing both BFS and FA for AACM production exhibits a synergistic effect, which could improve the mechanical properties and stability.[1,23]

The stability and mechanical properties of AACM are influenced by the dosage and composition of alkaline activating agents. Researchers investigated the impact of various factors on AACM strength. Chen *et al.* 2021 (ref. 24) analyzed the effects of alkali dosage (4–8%) and water glass modulus (0.5, 1.0, 1.5, 2.0) on the self-shrinkage ability of BFS-AACM. They noted that as the modulus increased, the self-shrinkage ability initially rose before declining. Additionally, an excess of silicate in the activator hindered internal water consumption, reducing the material's self-shrinkage ability. Likewise, the liquid–solid ratio for material preparation and the initial 24 h curing temperature also influenced the reaction. Muhammad *et al.* 2018 (ref. 25) discovered that water acted as the carrier of the alkaline activator, but higher water content diluted the alkali solution and generated larger pores, impacting curing strength. Zeng *et al.* 2022 (ref. 26) established that variations in the initial curing temperature affect the final compressive strength by influencing porosity.

Therefore, a composite alkali-activated cementitious materials (B–F-AACM) was prepared using BFS and FA for S/S of COPR. The single-factor experiment was conducted to investigate the impact of various factors on compressive strength, including water glass modulus, liquid–solid ratio, alkali-solid content, and curing temperature (24 hours prior). The mechanical strength and stability of the solidified body were evaluated through compressive strength test and leaching behavior analysis. Solidified body was characterized by the XRD, FTIR, and SEM techniques to further analyze the solidification mechanism.

2. Materials and methods

2.1 Materials

Respectively, the BFS and FA utilized in this experiment were brought from Ji Yuan steel factory and Da Tang power plant in Henan, China. While, the COPR was obtained from a chemical plant located in Chongqing, China. The analytical grade alkali activators were used in this study which were sodium silicate ($Na_2SiO_3 \cdot 3.3H_2O$) and sodium hydroxide (NaOH). Deionized water was utilized throughout all experiments conducted. XRF analysis was performed to determine the chemical composition of BFS, FA, and COPR. The results were presented in Table S1.† BFS primarily consisted of CaO, SiO_2, and Al_2O_3, which accounted for 82.37% of the total components; whereas FA mainly comprised SiO_2, Al_2O_3, and Fe_2O_3 components. COPR contained Fe_2O_3 (52.92%), Al_2O_3 (14.88%), MgO (10.55%), and Cr_2O_3 (10.53%) as its major constituents. Moreover, Fe in COPR was presented as Fe(III) according to the XPS spectra in Fig. S1(a).†

2.2 Methods

2.2.1 Preparation of AACM. The AACM was prepared by activating BFS and FA with a compound alkali activator

(Na_2SiO_3 and NaOH). Huang *et al.* 2017 (ref. 1) found that the addition of FA can significantly improve the fluidity and setting time of alkali-activated BFS binder. In this experiment, BFS as the main component, the addition of FA accounts for 5%. A single-factor experiment was conducted to examine the effects of water glass modulus (A1–A6), liquid–solid ratio (B1–B4), alkali-solid content (C1–C5), and initial 24 h curing temperature (D1–D4) on the compressive strength. The 19 samples each with three replicates ($19 \times 3 = 57$) were prepared according to single-factor experiment and layout given in Table 2. The experimental design divided the samples into four groups: A1–A6, B1–B4, C1–C5, and D1–D4. Each group tested the influence of one variable: group A (A1–A6) adjusted the water glass modulus from 1.0 to 2.0, keeping other conditions unchanged (liquid–solid ratio = 0.26, alkali–solid content = 6%, curing temperature = 30 °C). Similarly, group B (B1–B4) changed the liquid–solid ratio, group C (C1–C5) adjusted the alkali content, and group D (D1–D4) controlled the curing temperature. Other conditions remained unchanged.

Prior to the experiment, BFS and FA were dried at 105 °C for 5 h and passed through a 200-mesh sieve to ensure uniform particle size distribution. The alkali activators (Na_2SiO_3 and NaOH) solution were mixed in certain proportion with BFS and FA for certain period of time. The resulting mixture was quickly stirred to form a colloidal substance before being poured into a cube mold measuring 20 mm × 20 mm × 20 mm. Vibration was applied for approximately 1 min to remove internal bubbles from the colloidal paste. Subsequently, the samples were kept at temperatures of 30 °C, 45 °C, 60 °C, and 75 °C for a duration of 24 h. After this initial curing period, the demolding process was carried out. Afterwards, the samples were left at room temperature for an additional 27 days. Finally, the optimum conditions were determined based on the highest compressive strength observed during the single-factor experimental analysis.

Table 2 Single-factor experimental layout[a]

ID	Water glass modulus	Liquid–solid ratio	Alkali–solid content (%)	Curing temperature (°C)
A1	1.0	0.26	6	30
A2	1.2	0.26	6	30
A3	1.4	0.26	6	30
A4	1.6	0.26	6	30
A5	1.8	0.26	6	30
A6	2.0	0.26	6	30
B1	1.4	0.24	6	30
B2	1.4	0.26	6	30
B3	1.4	0.28	6	30
B4	1.4	0.30	6	30
C1	1.4	0.26	2	30
C2	1.4	0.26	4	30
C3	1.4	0.26	6	30
C4	1.4	0.26	8	30
C5	1.4	0.26	10	30
D1	1.4	0.26	6	30
D2	1.4	0.26	6	45
D3	1.4	0.26	6	60
D4	1.4	0.26	6	75

[a] Alkali–solid content: percentage of alkali–solid (Na_2SiO_3 and NaOH) in total solids; liquid–solid ratio: the ratio of water (deionized water and water in water glass) to total solids.

2.2.2 Solidification/stabilization (S/S) of COPR. The contents of CaO and SiO_2 in COPR are much less than those in BFS and FA, and COPR lacks alkali-activated cementitious properties. BFS and FA are utilized as alkali-activated cementitious material for COPR solidification/stabilization.

The COPR was solidified with the optimal combination of AACM (achieved through section 2.2.1). Various proportions (10%, 20%, 30%, 40%, 50% and 60%) of COPR, following a 5 hour drying process at 105 °C, were solidified into the composite alkali-activated cementitious materials, the COPR solidified bodies were named W10–W60, respectively. The amount of the alkaline activator used in Table S2.†

2.2.3 Compressive strength tests. The average compressive strength of three sets of 28 days solidified bodies were tested by using a pressure testing machine (YAW-1000, Hengsi Shengda, China).

2.2.4 Leaching tests. The solidification efficiency of the solidified body was tested using two leaching methods. These methods include: (1) sulfuric and nitric acid method (SNAM), following China Environmental Protection Standard HJ/T 299-2007.[27] This method simulated the chemical changes that occur in a solidified body (used as a construction material) when exposed to natural environmental factors like acid rain. (2) Toxicity characteristic leaching procedure (TCLP) stipulated by the US EPA method 1311 (1992).[28] The experiment simulated the release of toxic substances from the solidified body under underground storage conditions (used for landfill purposes). For the SNAM, crushed solidified body (<9.5 mm) were immersed in an extraction solution and shaken for 18 hours at a rate of 30 rpm using a rotary oscillation device. The extraction solution was prepared by mixing H_2SO_4 and HNO_3 in a mass ratio of 2 : 1, while maintaining a pH at 3.20 ± 0.05 and a liquid–solid ratio of 10 : 1. After extraction, the filtrate obtained through filtration using microporous filter paper (size range: 0.6–0.8 μm) was preserved with HNO_3 to maintain a pH below 2. TCLP was almost identical to the above method, except for using an acetic acid solution with a pH value of 2.88 ± 0.05 and a liquid–solid ratio of 20 : 1 for extraction. The content of Cr(VI) was determined by spectrophotometer according to GB/T15555.4-1995 standard.[29] The total chromium content was determined by flame atomic absorption spectrometer (FAAS) following HJ 749-2015 standard.[30]

2.2.5 Characterization analysis. The chemical composition of raw materials were determined by XRF (Panalytical Axios, Holland). The mineral phases were investigated by XRD (X 'Pert POWDER, PANalytical B. V., Holland) with CuK_α radiation in the 2θ range from 10° to 90°, generated at 30 mA and 40 KV. The XPS (ESCALAB Xi+, Thermo Scientific, USA) was used to measure the surface valence of Cr and Fe within COPR. The surface morphology of the solidified body was analyzed by SEM (JSM-6390LA, JEOL, Japan). The structure of the sample was quantified using FTIR (Nicolet iS20, Thermo Scientific, USA) in the range 400–4000 cm^{-1}. All XRD, SEM and FTIR measurements were taken at the age of 28 days.

3. Results and discussion

3.1 Compressive strength influenced by single-factor experiment

The experiment investigated the impact of water glass modulus, liquid–solid ratio, alkali-solid content, and initial 24 h curing temperature on compressive strength, which were given below.

3.1.1 Water glass modulus (SiO_2/Na_2O ratio). The water glass modulus refers to the molar ratio of SiO_2 to Na_2O in the alkali activator. The experiment explored the optimal ratio between water glass and sodium hydroxide by modifying the water glass modulus using NaOH. For this purpose, six different sets of water glass modules (A1 = 1.0, A2 = 1.2, A3 = 1.4, A4 = 1.6, A5 = 1.8, A6 = 2.0) were employed. As shown in Fig. 1(a)., the compressive strength initially decreased and then increased with a rise in the water glass modulus until it peaked at 88.8 MPa at A1 (modulus = 1). As the water glass modulus increased (>1), more soluble Si was released by the compound, promoting the formation of gelling material. However, this trend led to a reduction in the concentration levels of NaOH, resulting in incomplete or partial dissolution of the raw material within an alkaline environment. This slowdown impacted the increment of compressive strength and even led to a downward trend.[31,32] Huang *et al.* 2017 (ref. 1) demonstrated that appropriate ratios between SiO_2 and Na_2O can lead to increased compressive strength. Therefore, the water glass modulus of 1.0 was the best concentration of alkali activator.

3.1.2 Liquid–solid ratio. The liquid–solid ratio refers to the proportion of total liquid (water in water glass and deionized water) to solid material. The liquid–solid ratios of B1–B4 were 0.24, 0.26, 0.28, and 3.0, respectively. Water is an important component in the ongoing hydration reaction, and it plays a significant role in the alkali-activated process.[13] Sun *et al.* 2022 (ref. 21 and 23) concluded that an appropriate water content was beneficial for the hydrolytic condensation of materials and promoted the formation of a high-density and high-compressive strength solidified body. As depicted in Fig. 1(b), the compressive strength of the solidified body fluctuated with changes in the liquid–solid ratio. At a low liquid–solid ratio (<0.28), insufficient water content limited contact between the alkali activator and raw material, restricting the formation of solidified bodies. Conversely, when the liquid–solid ratio

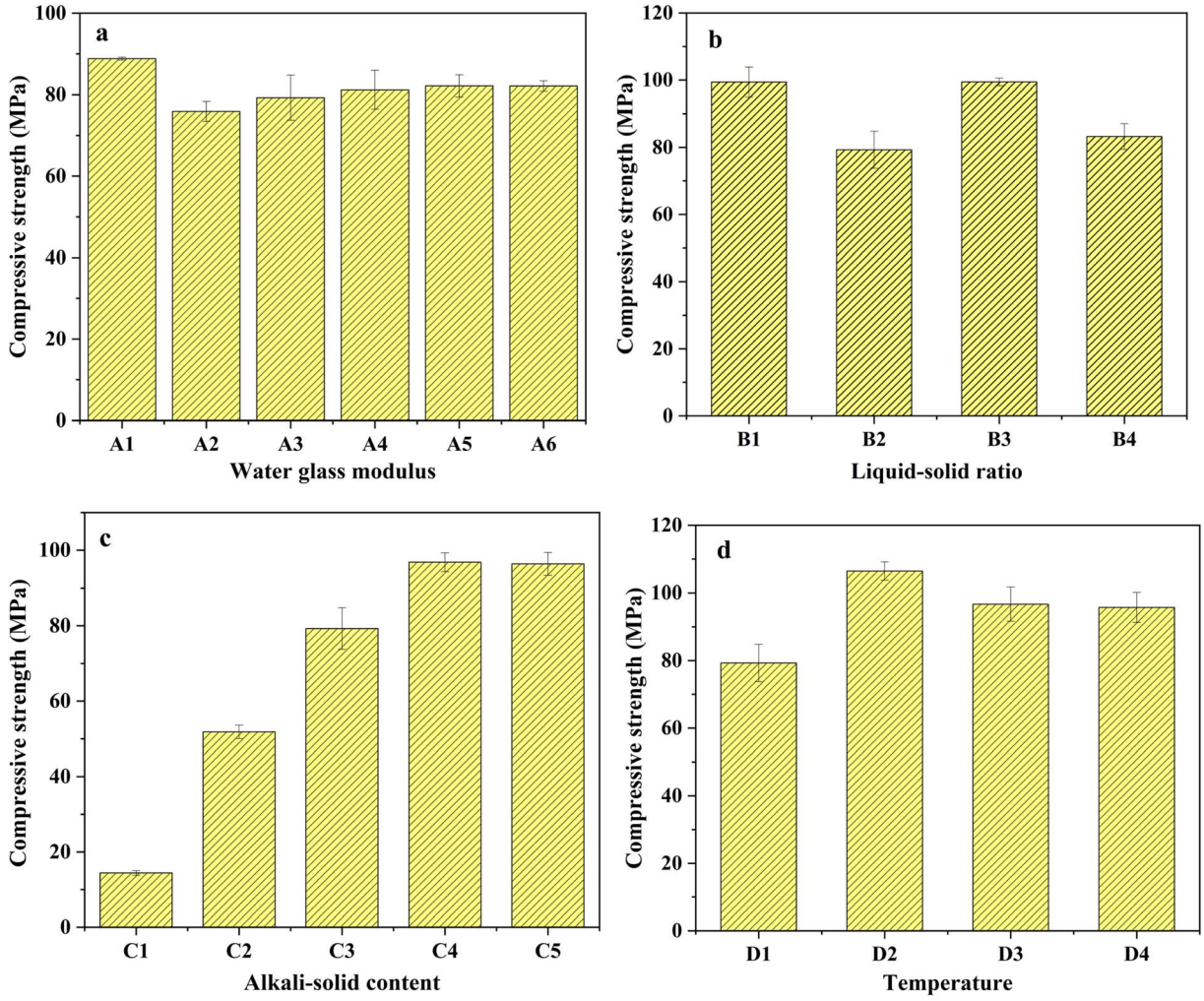

Fig. 1 The compressive strength of solidified bodies in the single-factor experiment: (a) water glass modulus; (b) liquid–solid ratio; (c) alkali–solid content; (d) curing temperature.

exceeded 0.28, there was a significant reduction in compressive strength due to dilution effects. Increasing water content reduced NaOH concentration, negatively impacting aluminosilicate dissolution and increasing porosity, which led to decreased compressive strength.[25] Fig. 1(b) showed that the maximum compressive strength (99.43 MPa) occurred at a liquid–solid ratio of 0.28, indicating an equilibrium state that promotes polycondensation reactions within gelled materials.

3.1.3 Alkali–solid content. The alkali-solid content refers to the proportion of the solid component in the alkali activator (the solids in $Na_2SiO_3 \cdot 3.3H_2O$ and NaOH) to the total solid component. As shown in Fig. 1(c), the compressive strength initially increases and then decreases as the alkali–solid content increases (C1 = 2%, C2 = 4%, C3 = 6%, C4 = 8% and C5 = 10%), reaching a maximum value of 96.8 MPa at C4 (8%). Higher alkali concentration promoted the dissolution of BFS-FA and led to a release of soluble Ca, Al, Si, and other substances, which increased the rate of C–S–H gel formation. While the alkali-solid content reached 10%, there was a slight decrease in compressive strength (96.3 MPa). This finding was consistent with previous experimental results.[5,19,33] It indicated that an excessive OH^- concentration hindered the dissolution of $Ca(OH)_2$ formed by BFS reaction, and a thin layer of $Ca(OH)_2$ was formed on the surface of BFS. Consequently, this impaired Ca's ability to react with Si and Al to form C–A–S–H gel. Moreover, an excess amount of OH^- can cause Al–Si gel precipitation on FA particle surfaces which further impeded the polycondensation reaction.[23]

3.1.4 Curing temperature. In this part, the influence of different temperatures (D1 = 30 °C, D2 = 45 °C, D3 = 60 °C, and D4 = 75 °C) on the compressive strength of AACM was investigated. As depicted in Fig. 1(d), the maximum compressive strength at D2 (45 °C) was recorded as 106.4 MPa. A gradual increase in temperature (<45 °C) favored an enhancement in compressive strength. This phenomenon can be attributed to the fact that elevated temperatures promote alkaline activator dissolution and the reaction of hydration reactions, thereby facilitating C–S–H gel structure formation.[34,35] While the temperature exceeded a certain threshold (>45 °C), there was a decline in compressive strength, which could be caused by an increased number of sulfate ions capable of reversibly binding with C–S–H gel.[36] Moreover, higher curing temperatures led to water evaporation in AACM, causing increased porosity and ultimately reducing its compressive strength. Henceforth, it can be concluded that the initial 24 h curing temperature exerts a significant influence on the final compressive strength achieved by solidified bodies.

3.2 Solidification/stabilization (S/S) of COPR

3.2.1 The compressive strength of solidified bodies containing COPR. To investigate the solidifying ability of AACM for COPR, COPR solidified bodies were prepared under optimized single-factor conditions (water glass modulus 1.0, liquid–solid ratio 0.28, alkali–solid content 8%, curing temperature 45 °C). Fig. 2 illustrated that the compressive strength measured without COPR at 147.8 MPa. However, with the addition of

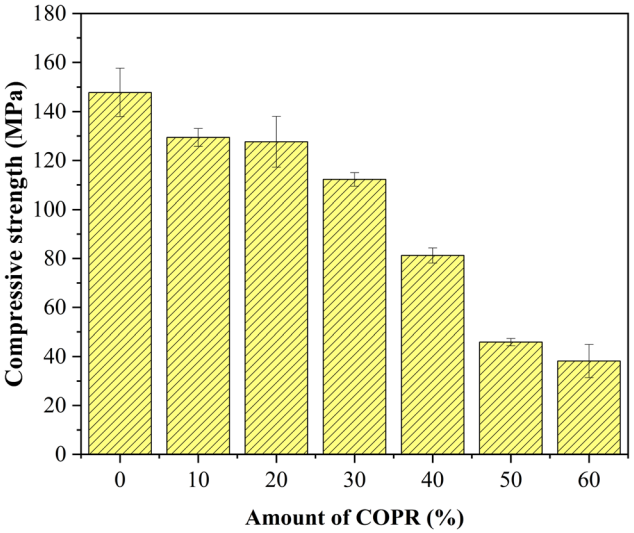

Fig. 2 The compressive strength of solidified bodies containing COPR.

COPR (10–60%), a significant decrease in the compressive strength of the solidified body was observed. This can be attributed to the fact that COPR lacks reactivity, and its increased proportion led to a reduction in BFS-FA content within the system, hindering sufficient reaction progress.[1] Furthermore, Xie *et al.* 2023 (ref. 37) discovered that heavy metals decreased mechanical properties in solidified bodies. Notably, W60 exhibited an impressive compressive strength value of up to 38.2 MPa with 60% COPR addition, meeting the standards for building material (>10.8 MPa) and landfill treatment requirements (>0.35 MPa). These findings indicated that the utilization of solidified products in construction applications was promising.

3.2.2 Leaching tests. The leaching tests were conducted using the sulfuric and nitric acid method (SNAM), as well as the Toxicity Characteristic Leaching Procedure (TCLP). By utilizing different acids, it was possible to assess the chemical stability of AACM in various aggressive environments. Table S3† presented the leaching concentrations of raw COPR and COPR solidified bodies (10–60% addition COPR). Generally, Fig. 3 illustrated that the leaching concentrations of Cr(VI) and total Cr in COPR solidified bodies increased with addition of COPR in the tests SNAM and TCLP. In the SNAM, the leaching concentrations of Cr(VI) and total Cr in COPR were 67.39 μg mL^{-1} and 81.24 μg mL^{-1} respectively (Table S3†)—both significantly exceeding the concentration limits of Cr(VI) (5.0 μg mL^{-1}) and total Cr (15 μg mL^{-1}). However, the leaching concentration of Cr(VI) in solidified body with 50% COPR decreased to 2.96 μg mL^{-1}, which fell below the limit value. In addition, the leaching concentration of total Cr (7.63 μg mL^{-1}) in W60 samples was much lower than its limit value as well. The results were consistent with previous observations by Huang *et al.* 2017.[1] The TCLP testing results (Fig. 4) demonstrated that as addition of COPR reached 60%, both Cr(VI) and total Cr levels in W60 samples were far below their respective limit values. The leaching tests results were

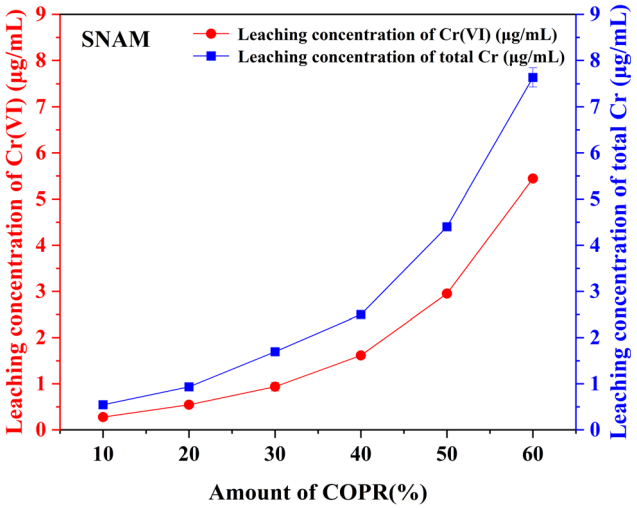

Fig. 3 The concentration of Cr(VI) and total Cr leached from solidified samples through SNAM.

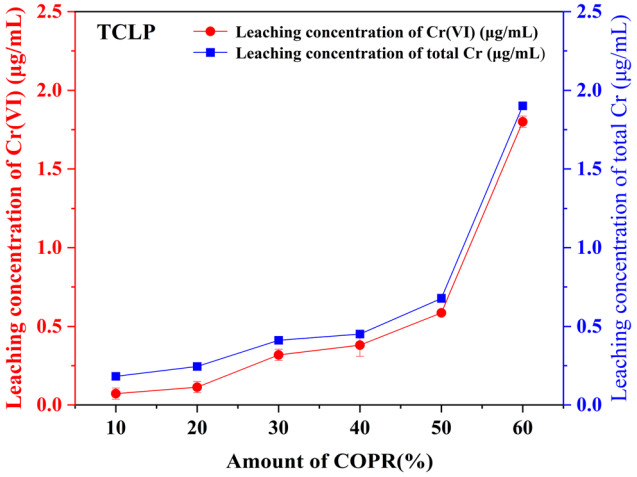

Fig. 4 The concentration of Cr(VI) and total Cr leached from solidified samples through TCLP.

consistent with XPS. The XPS spectra of COPR (Fig. S1(b)†) indicated that the original COPR contained both Cr(III) (78.91%) and Cr(VI) (21.09%), primarily with Cr(III) being predominant. All in all, the low level of Cr(VI) and total Cr leaching concentrations meant that Cr were not only immobilized by physical means but also by chemical ways.

Based on the results of leaching tests and XPS. It was speculated that Cr(VI) was reduced by reducing substances (such as S^{2-}) contained in BFS, resulting in an increase in the proportion of Cr(III) (eqn (1)).[38] As the Cr(III) was transformed and accumulated, it reacted with other substances to form insoluble compounds under alkaline conditions (eqn (2)). After precipitation, these compounds are physically wrapped in the solidified body and exist in a stable form, thereby reducing the harm of Cr(VI) in COPR.

$$3S^{2-} + 8CrO_4^{2-} + 20H_2O \rightarrow 3SO_4^{2-} + 8Cr^{3+} + 40OH^- \quad (1)$$

$$Cr + 3OH^- \rightarrow Cr(OH)_3 \quad (2)$$

3.3 The X-ray diffraction (XRD) analysis

The XRD patterns of the raw materials (BFS, FA, and COPR) were presented in Fig. 5. BFS exhibited a broad and weak peak appearing around 2θ of 25°–35°, indicating its amorphous, and only has a minor presence of gehlenite phase (PDF# 35-0755). The primary phases observed in FA were mullite (PDF# 79-1276) and quartz (PDF# 82-0211). In COPR, magnesium aluminum iron oxide ($MgFeAlO_4$, PDF# 11-0009) and magnesium chromium oxide ($MgCr_2O_4$, PDF# 77-0007) were the main phases detected, further suggesting a limited supply of alkali-activating substances from COPR. Fig. 6 illustrated the XRD patterns of the solidified bodies containing COPR. The strength of the amorphous hump in W0 (without COPR) increased and shifted to higher angles, signifying the formation of a new amorphous phase material. According to the study conducted by Huang

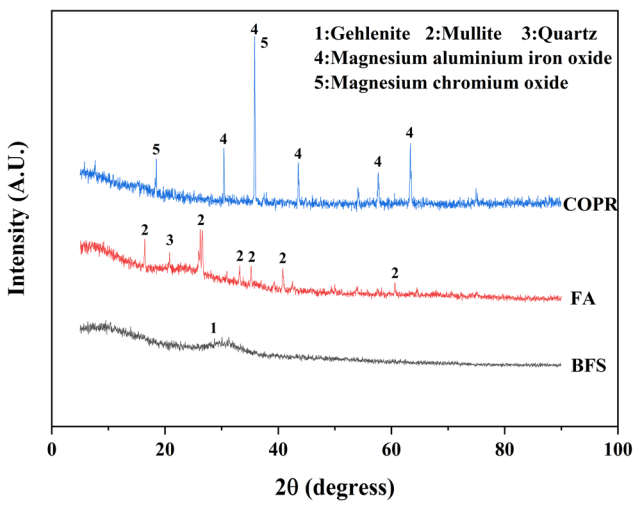

Fig. 5 The XRD patterns of COPR, FA and BFS.

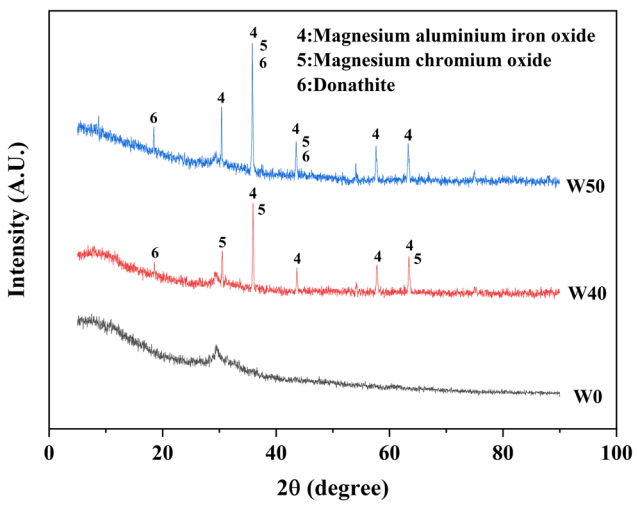

Fig. 6 The XRD patterns of COPR solidified bodies (W0, W40, W50).

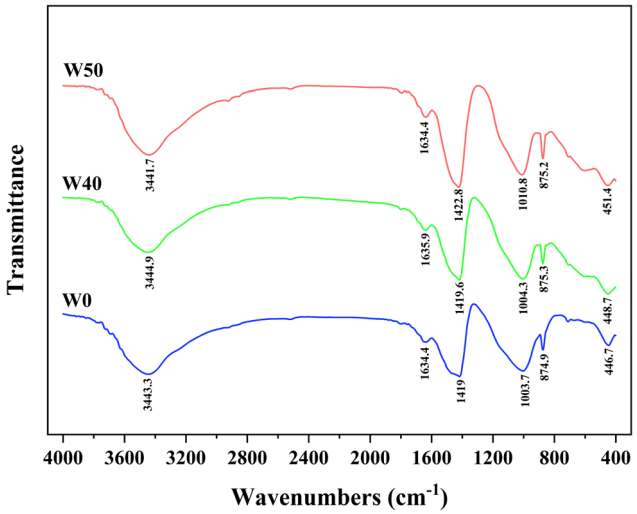

Fig. 7 The FTIR spectra of COPR solidified bodies (W0, W40, W50).

et al. 2017 (ref. 1) and Puertas *et al.* 2011,[20] it can be inferred that the formation of C–S–H gel structure occurred. The alkali activator facilitated the dissolution and recombination of Ca, Al, and Si substances abundant in BFS and FA, leading to the formation of C–S–H gel. Xia *et al.* 2020 (ref. 32) also discovered that the crystallinity of C–S–H phase was relatively low in AACM, with an increase in peak intensity over time. The XRD patterns of W40 and W50 exhibited remarkable similarities, both containing magnesium aluminum iron oxide and magnesium chromium oxide found in COPR. Additionally, a small amount of donathite ($(Fe, Mg)(Cr, Fe)_2O_4$, PDF# 22-0349) was present, indicating potential binding between chromium ions and silicates in an amorphous state.

3.4 Fourier transform infrared spectroscopy (FTIR) analysis

In order to gain a deeper understanding of the internal structural changes in solidified bodies and the solidification

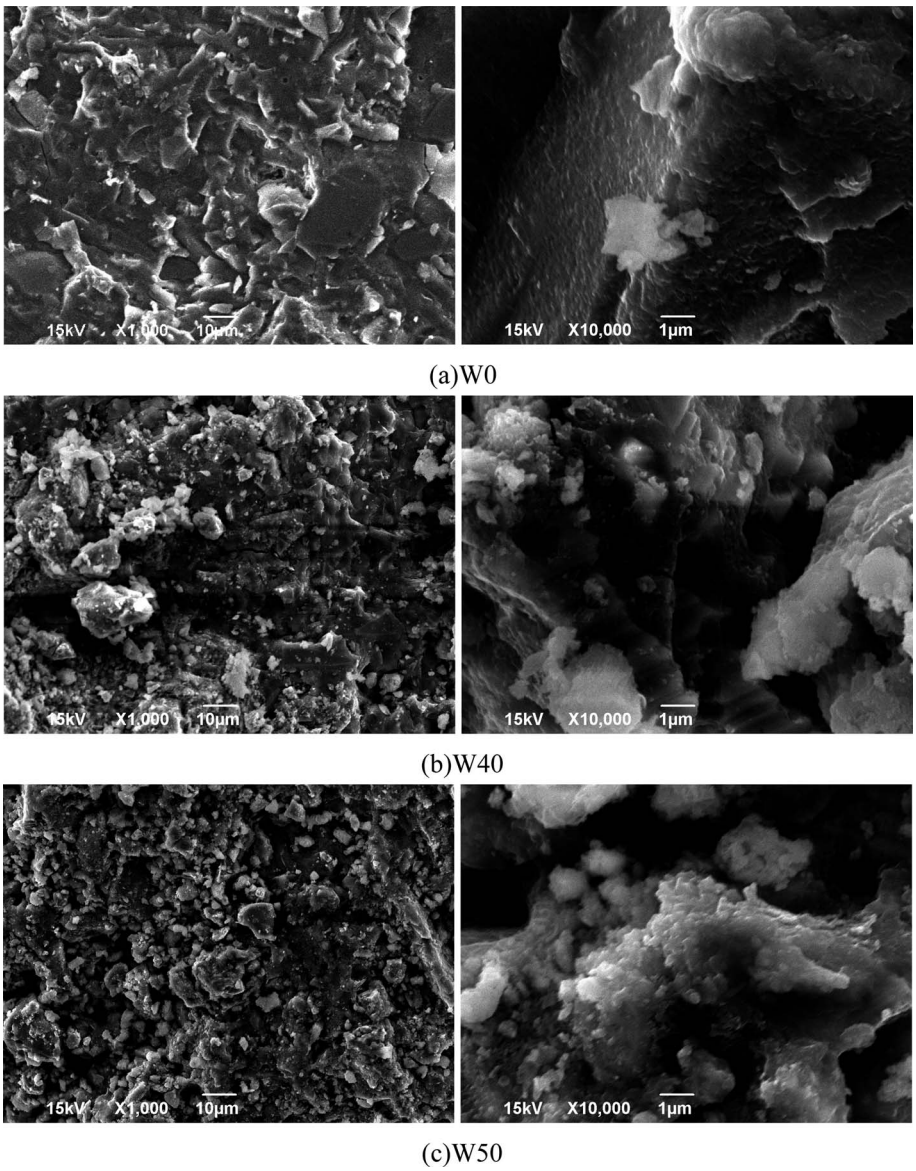

Fig. 8 The SEM micrographs of solidified bodies: (a) W0; (b) W40; (c) W50.

mechanism of heavy metal chromium after 28 days, FTIR was employed for analysis. As depicted in Fig. 7, the FTIR spectra of solidified bodies without COPR (W0) and those with COPR (W40, W50) exhibited similar characteristics. The absorption peak at 3400–3500 cm^{-1} corresponded to the OH stretching vibration.[39] The absorption peak within the range of 1600–1650 cm^{-1} was attributed to the bending vibration of OH caused by H_2O molecule adsorption on the solidified body,[13,25,39] indicating the presence of water molecules in the solidified bodies. The antisymmetric stretching band at 1410–1430 cm^{-1} corresponded to O–C–O bond stretching vibrations,[40] which was induced by CO_2 participating in alkali activation processes leading to carbonate formation.[13,35] The band near 1000 cm^{-1} was associated with antisymmetric stretching of Si–O–T bonds (T = tetrahedral Si or Al) in reaction products,[40] with a shift towards higher wave numbers as COPR was added. This may be due to heavy metal chromium forming chemical bonds with aluminosilicate gel, resulting in a higher wave number absorption peak for Si–O–T bonding.[41] Since increased COPR content reduced the Si/Al ratio among reactants. Therefore, there was a higher proportion of Si–O–Al compared to Si–O–Si bonds. Since Si–O–Al bonds were weaker than Si–O–Si bonds, network materials formed became more prone to fracture, thus exhibiting decreasing compressive strength trends.[21]

The peak near 875 cm^{-1} related to antisymmetric stretching vibrations from AlO_4^- groups while that near 450 cm^{-1} pertained to bending vibrations from Si–O–Si and O–Si–O bonds.[26,40] It can be observed from Fig. 7 that peaks within both ranges shift towards higher wave numbers. The shift to a higher wave number indicated that the presence of contaminant ions impacts the molecular structure of the solidified body.[32] This could be attributed to either the substitution of Si by Cr in the gel structure or the influence of Cr on the C–S–H gel structure, altering the degree of gel polymerization.[26] Consequently, compared to W40, there was an increase in leaching concentration of Cr(VI) and a decrease in compressive strength observed in W50.

3.5 Scanning electron microscopy (SEM). The microstructure of the solidified body was examined by using SEM. W0 in Fig. 8(a) illustrated a dense internal structure of the solidified body, while the surface exhibits a layered structure with attached white colloidal material. This white colloidal structure might be a product of hydrated C–S–H gel or N–A–S–H gel, which could fill microcracks to enhance the solidity of the structure and reinforce the mechanical performance.[1] However, upon addition of COPR, as depicted in Fig. 8(b) and (c), significant changes have occurred in the solidified body's structure. More pores and microcracks became evident on the surface. The addition of COPR disrupted the compact microstructure of the solidified body. Moreover, numerous small circular aggregates were observed on the surface, and indicated it was unreacted FA. The increase in COPR hindered the complete dissolution and release of Si and Al from raw materials within an alkaline environment, thereby impeding polymerization reaction.[13,25] Furthermore, heavy metal chromium was possibly fixed in C–S–H gel structures by physical mean. Ultimately, this led to a decrease in compressive strength and an increase in the leaching content of Cr(VI).

4. Conclusions

In this study, alkali activated BFS and FA were utilized for the preparation of AACM, and solidification/stabilization of COPR. A small amount of FA (5%) was added to BFS as a micro aggregate to create a denser internal structure within the solidified bodies. To optimize the formation condition for AACM, single-factor experiments were conducted with compressive strength as the evaluative index. Furthermore, the efficiency of the solidified body's stabilization/solidification process was assessed based on both its compressive strength and the leaching concentration of heavy metal Cr (Cr(VI) and total Cr). The physicochemical structure and microstructure analyses of the solidified bodies were performed using XRD, FTIR, and SEM techniques. Based on these analyses, the following conclusions were drawn.

(1) With water glass modulus 1.0, liquid–solid ratio 0.28, alkali-solid content 8%, and curing temperature 45 °C, the maximum compressive strength reached 147.8 MPa for solidified samples (28 days). The addition of COPR led to a continuous decrease in the compressive strength of the solidified bodies. Even 60% addition COPR, W60 samples still exhibited favorable mechanical properties (38.2 MPa), which met the requirements for building material. The leaching results of COPR solidified bodies (≤50% COPR) in those methods (SNAM and TCLP) were below limit values, which demonstrated a significant immobilization effect on Cr(VI) and total Cr in the B–F-AACM solidified bodies compared to raw COPR. The results of leaching tests and XPS showed that the stability of Cr(VI) in the solidified body was due to the combined effects of physical and chemical processes. The chemical processes primarily include the reduction of Cr(VI) and the co-precipitation of Cr(III).

(2) The lower leaching concentration results, along with XRD, SEM, and FTIR analysis showed that the amorphous C–S–H gel structure was formed by alkali activation of BFS and FA. This gel structure exhibited high density and stability. While the addition of COPR disrupted the dense structure and caused a shift in the absorption peak observed in the FTIR spectra, indicating the presence of Cr influenced the molecular arrangement within the solidified body through chemical bonding. Furthermore, SEM images revealed that COPR could be physically immobilized within the gel structure of AACM. Therefore, the AACM can effectively handle COPR by employing both physical fixation and chemical reactions to securely immobilize chromium.

Abbreviations

COPR	Chromite ore processing residue
BFS	Blast furnace slag
AACM	Alkali-activated cementitious materials
LZSS	Lead and zinc smelting slag
BFS-AACM	Preparation of AACM using BFS

C–(A)–S–H	$CaO–Al_2O_3–SiO_2–H_2O$
B–F-AACM	Preparation of the compose AACM using BFS and FA
TCLP	Toxicity characteristic leaching procedure
S/S	Solidification/stabilization
FA	Fly ash
OPC	Ordinary Portland cement
LSS	Lead smelting slag
FA-AACM	Preparation of AACM using FA
N–A–S–H	$NaO_2–Al_2O_3–SiO_2–H_2O$
C–S–H	$CaO–SiO_2–H_2O$
SNAM	Sulfuric and nitric acid method

Data availability

The date underlying this article are available in the article and its online ESI.†

Author contributions

Pengyue Su: methodology, investigation, formal analysis, writing-original draft. Pan Zhao: writing-review & editing. Hao Wang: software, visualization. Kun Zhou: resources. Yicheng Guo: validation. Sha Liu: validation. Huicheng Lu: writing-review & editing. Haiyu Chen: funding acquisition. Lanjun Zhang: project administration. Ziqiang He: project administration. Ming Xia: conceptualization, project administration and funding acquisition. Shujie Zhao: supervision.

Conflicts of interest

There are no conflicts of interest to declare.

Acknowledgements

This study was supported by the Natural Science Foundation of Jiangsu Province (Grant No. BK20210926), National Natural Science Foundation of China (No. 52304196) and Jiangsu Ocean University Talent Introduction Start-up Fund (No. KQ21007). It was also funded by Innovation and Entrepreneurship Training Program for College Students (SY202111641637017, SZ202111641637004, SY202211641637014) and Postgraduate Research and Practice Innovation Program of Jiangsu Ocean University (KYCX2023-15). Supported by Open-end Funds of Jiangsu Key Laboratory of Function Control Technology for Advanced Materials, Jiangsu Ocean University (JSKLFCTAM202006) and Open-end Funds of Jiangsu Institute of Marine Resources Development (JSIMR202020).

References

1 X. Huang, R. Zhuang, F. Muhammad, L. Yu, Y. Shiau and D. Li, *Chemosphere*, 2017, **168**, 300–308.
2 X. Chuai, R. Xiao, L. Chang, J. Wang, H. Yong, R. Jiang, T. Zhang, S. Tan, Y. Zhao, Z. Xiong and J. Zhang, *J. Hazard. Mater.*, 2022, **431**, 128656.
3 J. Ge, Y. Xiao, J. Kuang and X. Liu, *Surf. Interfaces*, 2022, **29**, 101744.
4 S. S. Rath, P. Nayak, P. S. Mukherjee, G. Roy Chaudhury and B. K. Mishra, *Waste Manage.*, 2012, **32**, 575–583.
5 N. Li, C. Shi, Z. Zhang, D. Zhu, H.-J. Hwang, Y. Zhu and T. Sun, *Cem. Concr. Compos.*, 2018, **93**, 163–174.
6 Y. Li, J. Liang, Z. Yang, H. Wang and Y. Liu, *Sci. Total Environ.*, 2019, **658**, 315–323.
7 P. Zhang, L. Zeng, S. Zhang, C. Li and D. Li, *Environ. Sci. Pollut. Res.*, 2022, **30**, 29392–29406.
8 M. He, F. Wu, G. Qu and X. Liu, *Environ. Res.*, 2023, **238**, 117149.
9 C. Jin, J. Yang, B. Chen, G. Qu, H. Li, F. Wu, X. Liu, Y. Liu, L. Kuang and J. Li, *Environ. Res.*, 2023, **236**, 116856.
10 A. B. Saralegui, V. Willson, N. Caracciolo, M. N. Piol and S. P. Boeykens, *J. Environ. Manage.*, 2021, **289**, 112398.
11 C. Shi and A. Fernández-Jiménez, *J. Hazard. Mater.*, 2006, **137**, 1656–1663.
12 I.-H. Yoon, D. H. Moon, K.-W. Kim, K.-Y. Lee, J.-H. Lee and M. G. Kim, *J. Environ. Manage.*, 2010, **91**, 2322–2328.
13 M. Xia, F. Muhammad, L. Zeng, S. Li, X. Huang, B. Jiao, Y. Shiau and D. Li, *J. Cleaner Prod.*, 2019, **209**, 1206–1215.
14 J. Davidovits, *J. Therm. Anal.*, 1991, **37**, 1633–1656.
15 L. Zhao, X. Ma, S. Song, P. You and H. Wu, *Constr. Build. Mater.*, 2022, **319**, 126091.
16 J. Zhang, Y. Ma, J. Zheng, J. Hu, J. Fu, Z. Zhang and H. Wang, *Constr. Build. Mater.*, 2020, **261**, 119940.
17 Z. Zhao, W. Liu, Y. Jiang, Y. Wan, R. Du and H. Li, *J. Cleaner Prod.*, 2022, **359**, 132134.
18 Y. Xing and B. Wang, *J. Build. Eng.*, 2023, **78**, 107573.
19 I. Ismail, S. A. Bernal, J. L. Provis, R. San Nicolas, S. Hamdan and J. S. J. van Deventer, *Cem. Concr. Compos.*, 2014, **45**, 125–135.
20 F. Puertas, M. Palacios, H. Manzano, J. S. Dolado, A. Rico and J. Rodríguez, *J. Eur. Ceram. Soc.*, 2011, **31**, 2043–2056.
21 B. Sun, G. Ye and G. de Schutter, *Constr. Build. Mater.*, 2022, **326**, 126843.
22 A. Mehta, R. Siddique, T. Ozbakkaloglu, F. Uddin Ahmed Shaikh and R. Belarbi, *Constr. Build. Mater.*, 2020, **257**, 119548.
23 G. Fang, Q. Wang and M. Zhang, *Composites, Part B*, 2021, **224**, 109221.
24 W. Chen, B. Li, J. Wang and N. Thom, *Cem. Concr. Res.*, 2021, **141**, 106322.
25 F. Muhammad, X. Huang, S. Li, M. Xia, M. Zhang, Q. Liu, M. A. Shehzad Hassan, B. Jiao, L. Yu and D. Li, *J. Cleaner Prod.*, 2018, **188**, 807–815.
26 L. Zeng, P. Zhang, J. Li, Q. Yu, Y. Zheng and D. Li, *Ecotoxicol. Environ. Saf.*, 2022, **247**, 114221.
27 CN-HJ, *Solid Waste-Extraction Procedure for Leaching Toxicity-Sulphuric Acid and Nitric Acid Method (HJ/T 299-2007)*, 2007.
28 US Environmental Protection Agency, *Toxicity Characteristic Leaching Procedure (Method 1311)*, 1992.
29 CN-GB, *Solid Waste-Determination of Chromium(VI)-1,5-Diphenylcarbohydrazide Spectrophotometric Method (GB/T 15555. 4-1995)*, 1995.

30 CN-HJ, *Solid Waste-Determination of Total Chromium-Flame Atomic Absorption Spectrometry (HJ 794-2015)*, 2015.
31 Z. Luo, T. Zhi, L. Liu, J. Mi, M. Zhang, C. Tian, Z. Si, X. Liu and Y. Mu, *Constr. Build. Mater.*, 2022, **316**, 125813.
32 M. Xia, F. Muhammad, S. Zhao, L. Yu, H. Lin, X. Huang, B. Jiao, Y. C. Shiau and D. Li, *J. Environ. Manage.*, 2020, **265**, 110350.
33 Z. Shi, C. Shi, S. Wan and Z. Zhang, *Cem. Concr. Res.*, 2018, **111**, 104–115.
34 H. Lahalle, V. Benavent, V. Trincal, T. Wattez, R. Bucher and M. Cyr, *Constr. Build. Mater.*, 2021, **300**, 124066.
35 L. Yu, L. Fang, P. Zhang, S. Zhao, B. Jiao and D. Li, *Int. J. Environ. Res. Public Health*, 2021, **18**, 9960.
36 O. R. Ogirigbo and L. Black, *Constr. Build. Mater.*, 2016, **126**, 496–507.
37 R. Xie, R. Ge, Z. Li, G. Qu, Y. Zhang, Y. Xu, Y. Zeng and Z. Li, *J. Environ. Manage.*, 2023, **325**, 116469.
38 X. Huang, Research on Solidification/stabilization of Chromite Ore Processing Residue Using Composite Materials Based Geopolymer and its Enhanced Technology, PhD thesis, Chongqing University, 2018.
39 C. Y. Heah, H. Kamarudin, A. M. Mustafa Al Bakri, M. Bnhussain, M. Luqman, I. Khairul Nizar, C. M. Ruzaidi and Y. M. Liew, *Constr. Build. Mater.*, 2012, **35**, 912–922.
40 S. A. Bernal, J. L. Provis, V. Rose and R. Mejía de Gutierrez, *Cem. Concr. Compos.*, 2011, **33**, 46–54.
41 J. Liu, G. Xie, Z. Wang, Z. Li, X. Fan, H. Jin, W. Zhang, F. Xing and L. Tang, *J. Environ. Manag.*, 2023, **341**, 118053.